



HAL
open science

Stochastic optimization of a mass-in-mass cell with piecewise hybrid nonlinear-linear restoring force

Camila da Silveira Zanin, Samy Missoum, Alireza Ture Savadkoohi, Sébastien Baguet, Emmanuel Gourdon, Régis Dufour

► **To cite this version:**

Camila da Silveira Zanin, Samy Missoum, Alireza Ture Savadkoohi, Sébastien Baguet, Emmanuel Gourdon, et al.. Stochastic optimization of a mass-in-mass cell with piecewise hybrid nonlinear-linear restoring force. *Journal of Sound and Vibration*, 2024, pp.118755. 10.1016/j.jsv.2024.118755 . hal-04736335

HAL Id: hal-04736335

<https://hal.science/hal-04736335v1>

Submitted on 14 Oct 2024

HAL is a multi-disciplinary open access archive for the deposit and dissemination of scientific research documents, whether they are published or not. The documents may come from teaching and research institutions in France or abroad, or from public or private research centers.

L'archive ouverte pluridisciplinaire **HAL**, est destinée au dépôt et à la diffusion de documents scientifiques de niveau recherche, publiés ou non, émanant des établissements d'enseignement et de recherche français ou étrangers, des laboratoires publics ou privés.

Stochastic optimization of a mass-in-mass cell with piecewise hybrid nonlinear-linear restoring force

C. da Silveira Zanin^{a,b,*}, S. Missoum^c, A. Ture Savadkoohi^a, S. Baguet^b, E. Gourdon^a, R. Dufour^b

^aUniv Lyon, ENTPE, LTDS UMR CNRS 5513, 69518 Vaulx-en-Velin, France

^bUniv Lyon, INSA Lyon, LaMCoS UMR CNRS 5259, 69621 Villeurbanne, France

^cAerospace and Mechanical Engineering Department. University of Arizona. Tucson, Arizona, USA

Abstract

This article investigates the optimization under uncertainty of a mass-in-mass meta-cell for its potential use within a metamaterial. The specificity of the proposed mass-in-mass system stems from the hybrid nonlinear-linear stiffness at the inner level. It is well known that these systems exhibit high sensitivity to small perturbations in loading conditions or design parameters. In fact, the sensitivity is such that the system can exhibit discontinuous behaviors. Therefore the proposed optimization approach not only accounts for sources of uncertainties but also can handle discontinuous responses. The objective of the stochastic optimization is to find the stiffness properties of the mass-in-mass system which minimize the expected value of a specific efficiency metric. In order to better understand the system's dynamic behavior and the origins of the discontinuities, slow invariant manifolds and frequency response curves are provided. [The efficiency of the optimized system with hybrid stiffness is compared with that of a similar optimized system featuring pure cubic nonlinearity.](#)

1. Introduction

Metamaterials are engineered systems that leverage various physical and mechanical properties at micro-scale to achieve tailored responses at macro-scale [1, 2, 3, 4]. Examples of such behaviors in mechanical metamaterials [5, 6] include zero or negative Poisson's ratio, mass, density, etc. [7, 8, 9, 10], and the emergence of bandgapsfrequency ranges where the system response to external excitation or waves is zero or stays below a controlled threshold [11, 12, 13]. One such designed system of interest in this paper is mass-in-mass cells [14, 15, 16], which can exhibit rich dynamical behaviors in linear [17] and nonlinear [18, 19] domains, characterized by the creation of bandgaps and modulated responses in linear and nonlinear domains, respectively. The inner mass of a single mass-in-mass cell can be tailored to design the responses of the outer mass, such as controlling its vibratory response and/or harvesting its energy.

The passive vibratory energy control of a dynamic system is typically achieved using a secondary oscillator whose linear or nonlinear characteristics are specifically tailored and exploited [20, 21]. The most established of such oscillators is referred to as a Frahm device [22] or tuned mass damper [23]. This device has a high efficiency near their tuned frequencies but degrades substantially elsewhere. To overcome this limitation, Roberson [24] introduced a cubic part to the linear restoring force, expanding its operational frequency range. Since then, different types of nonlinear passive absorbers have been developed, notably the nonlinear energy sink (NES) [25, 26, 27]. As research progressed, various other nonlinearities were explored, including nonsmooth systems such as vibro-impact [28, 29, 30], piece-wise linear models [31, 32, 33], and Bouc-Wen type nonlinearities [34]. In such systems, it is possible to induce an irreversible transfer of vibrational energy from the main oscillator to the nonlinear one, a phenomenon known as targeted energy transfer [25, 27, 35].

The NES design dictates the targeted energy transfer, including the possible bifurcations and, consequently, the NES efficiency to absorb and dissipate energy. However, it was observed that NESs exhibit a remarkable sensitivity

*Corresponding author - camila.zanin@entpe.fr

to perturbations in design parameters or initial conditions [36], sometimes leading to a discontinuous nature of activation, and even a slight alteration in these factors can trigger a change from a state of "high" to "low" efficiency. Therefore, given that the device must have specific properties and uncertainties can significantly affect its performance, an optimization process that accounts for sources of uncertainty becomes an essential task.

In this article, we present the optimization of a grounded cell composed of an outer mass housing an inner resonator with specific stiffness properties. The proposed mass-in-mass design is based on a hybrid nonlinear-linear stiffness whose characteristics are the subject of the proposed optimization. In addition, the optimization is stochastic in nature and accounts for various sources of uncertainties in design and loading.

To perform the stochastic optimization [37], this study employs the algorithm presented in [38], which is based on Kriging surrogate model [39], clustering [40], and a support vector machine (SVM) classifier [41]. The optimization scheme enables the unsupervised identification of regions with different levels of efficiency, such as in the case where the resonator is activated. The stochastic optimization methods enables the use of random design variables and random parameters (aleatory variables) such as the initial velocity of the outer mass or the excitation force magnitude. The objective function considered is the expected value of the amplitude of the main system for given ranges of excitation conditions, including cases where the main mass is subjected to an impulse or a harmonic force. In order to further understand the dynamics leading to the optimal results and the origin of the discontinuities, Slow Invariant Manifolds (SIM) and frequency response curves, as investigated in [18], are presented.

The article is constructed as follows: in Section 2, we introduce the system and its dynamics, along with the methods used to derive the SIM and the frequency response curves. This section also presents the efficiency metric and analysis of the system's activation levels, sources of incertitudes and potential discontinuous behavior. Section 3 describes optimization problem under uncertainty formulation and outlines the proposed algorithm for minimizing the mean efficiency. Additionally, this section introduces important tools such as Kriging and SVM. In Section 4, we present the optimization of the meta-cell, considering two types of excitation and two different nonlinearities for the system.

2. The system under study and its different dynamics

2.1. Academic model

A mass-in-mass cell unit is represented in Fig. 1. It consists of an outer rigid mass m_1 with generalized displacement $u_1(t)$ and an inner rigid mass m_2 having the generalized displacement $u_2(t)$. The outer mass is grounded by a linear spring with constant stiffness k_1 and linear damping with a constant coefficient c_1 . Both masses are coupled via a damping coefficient, c_2 , and a nonlinear restoring force, $F(\alpha)$, function of the relative displacement of the two masses. Besides that, the outer mass (m_1) is forced by an external sinusoidal excitation $S(t) = P \sin(\Omega t)$.

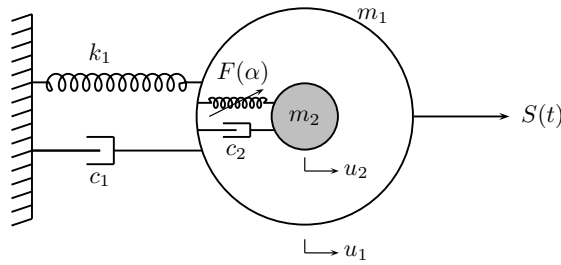


Figure 1: Model of a mass-in-mass cell unit [18]. The nonlinear interactions between two masses is represented by the function $F(\alpha)$.

The governing equations of the system in the time domain t are as follows:

$$\begin{cases} m_1 u_1'' + k_1 u_1 + c_1 u_1' + F(u_1 - u_2) + c_2(u_1' - u_2') = P \sin(\Omega t) \\ m_2 u_2'' + F(u_2 - u_1) + c_2(u_2' - u_1') = 0 \end{cases} \quad (1)$$

55 where $(\cdot)'$ stands for derivative with respect to t .
Introducing a dimensionless time τ as:

$$\tau = \omega t = \sqrt{\frac{k_1}{m_1}} t \quad (2)$$

The Eq. 1 adopts the dimensionless form:

$$\begin{cases} \ddot{u}_1 + u_1 + \epsilon \zeta_1 \dot{u}_1 + \epsilon f(u_1 - u_2) + \epsilon \zeta_2 (\dot{u}_1 - \dot{u}_2) = \epsilon \gamma \sin(\vartheta \tau) \\ \epsilon \ddot{u}_2 + \epsilon f(u_2 - u_1) + \epsilon \zeta_2 (\dot{u}_2 - \dot{u}_1) = 0 \end{cases} \quad (3)$$

where (\cdot) stands for the derivative with respect to τ .

ϵ is a physical parameter representing the mass ratio between the two oscillators, i.e., $\epsilon = m_2/m_1$. Assuming that
60 $0 < \epsilon \ll 1$, the following parameters are introduced:

$$\epsilon \zeta_1 = \frac{c_1}{\sqrt{k_1 m_1}}, \quad \epsilon \zeta_2 = \frac{c_2}{\sqrt{k_1 m_1}}, \quad \epsilon \gamma = \frac{P}{k_1}, \quad \vartheta = \frac{\Omega}{\omega}, \quad \epsilon f(u_1 - u_2) = \frac{F(u_1 - u_2)}{k_1} \quad (4)$$

$f(\alpha)$ is defined as:

$$f(\alpha) = \begin{cases} k_{NL} \alpha^3 & \text{if } -\delta \leq \alpha \leq \delta \\ k_L(\alpha - \delta) + k_{NL} \delta^3 & \text{if } \alpha > \delta \\ k_L(\alpha + \delta) - k_{NL} \delta^3 & \text{if } \alpha < -\delta \end{cases} \quad (5)$$

In detail, the restoring force function $f(\alpha)$ is cubic in the clearance of 2δ and it becomes linear elsewhere, with a slope of k_L .

The dynamical behavior of the system is studied by applying the multiple time scales method [42] combined with a
65 complexification method [43], which are the subject of the following subsection.

2.2. Multiple time scales methods and complex variables of Manevitch

In the multiple time scales method, the time scales τ_j are defined as follows [42]:

$$\tau_j = \epsilon^j \tau, j \in \mathbb{N} \quad (6)$$

Different scales of time are coupled to each other via the small physical parameter ϵ . The time is decomposed in fast
(τ_0) and slow scales ($\tau_j = \epsilon^j \tau, j = 1, 2, \dots$).

70 For further developments, new variables w and v , which correspond to the center of mass of the two particles and the relative displacement, respectively, will be introduced as [18]:

$$\begin{bmatrix} w \\ v \end{bmatrix} = \begin{bmatrix} 1 & \epsilon \\ 1 & -1 \end{bmatrix} \begin{bmatrix} u_1 \\ u_2 \end{bmatrix} \quad (7)$$

The multiple scales method will be combined with the complexification technique. Complex variables of Manevitch
[43], as function of the dimensionless frequency ϑ , are applied to the system as follows:

$$\begin{cases} \varphi_1 e^{i\vartheta \tau} = \dot{w} + i\vartheta w \\ \varphi_2 e^{i\vartheta \tau} = \dot{v} + i\vartheta v \end{cases} \quad (8)$$

with $i^2 = -1$.

75 To keep only the resonant terms corresponding to this pulsation, a Galerkin method is applied based on the truncated Fourier series via keeping the first harmonics. For a generic function $s(\varphi_1, \varphi_2, \varphi_1^*, \varphi_2^*)$, this task is carried out via:

$$S(\varphi_1, \varphi_2, \varphi_1^*, \varphi_2^*) = \frac{\vartheta}{2\pi} \int_0^{\frac{2\pi}{\vartheta}} s(\varphi_1, \varphi_2, \varphi_1^*, \varphi_2^*) e^{-i\vartheta \tau} d\tau \quad (9)$$

When using this technique, it will be assumed that $\varphi_1, \varphi_2, \varphi_1^*, \varphi_2^*$ do not depend on fast timescale, i.e., $\tau_0 = \tau$. The validity of this assumption is checked during the multiple scale analysis.

Applying the complex variables of Manevitch and the Galerkin method, the following system of equations is obtained:

$$\begin{cases} \frac{\dot{\varphi}_1}{2} + \frac{i\vartheta\varphi_1}{2} + \frac{1}{(1+\epsilon)}\frac{\varphi_1}{2i\vartheta} + \frac{\epsilon}{(1+\epsilon)}\frac{\varphi_2}{2i\vartheta} + \frac{\epsilon}{(1+\epsilon)}\zeta_1\left(\frac{\varphi_1}{2} + \epsilon\frac{\varphi_2}{2}\right) - \frac{\epsilon\gamma}{2i} = 0 \\ \frac{\dot{\varphi}_2}{2} + \frac{i\vartheta\varphi_2}{2} + \frac{1}{(1+\epsilon)}\frac{\varphi_1}{2i\vartheta} + \frac{\epsilon}{(1+\epsilon)}\frac{\varphi_2}{2i\vartheta} + \frac{\epsilon}{(1+\epsilon)}\zeta_1\left(\frac{\varphi_1}{2} + \epsilon\frac{\varphi_2}{2}\right) + \mathcal{F}(\varphi_2, \varphi_2^*)(\epsilon+1) + \zeta_2\frac{\varphi_2}{2}(\epsilon+1) - \frac{\epsilon\gamma}{2i} = 0 \end{cases} \quad (10)$$

In the subsequent subsection, we address Eq. (10) using the method of multiple scales via looking at equations of different orders of ϵ . Selected results from [18], accompanied by supplementary analysis, are also provided to a better understanding of the system's dynamics.

2.3. Fast and slow dynamics of the system

We consider the system behavior in the vicinity of 1:1 resonance, where the frequency of the main system is close to that of the external force. From that, we set $\vartheta = 1 + \sigma\epsilon$, where σ is the detuning parameter.

Fast dynamics. The system behavior at the fast time scale is described by the system of equations (10) at ϵ^0 order:

$$\begin{cases} \frac{\partial\varphi_1}{\partial\tau_0} = 0 \\ \frac{\partial\varphi_2}{\partial\tau_0} + i\varphi_2 - i\varphi_1 - i\varphi_2g(|\varphi_2|^2) + \zeta_2\varphi_2 = 0 \end{cases} \quad (11)$$

where [18]:

$$g(|\varphi_2|^2) = \begin{cases} \frac{3K_{NL}|\varphi_2|^2}{4} & \text{if } |\varphi_2| < \delta \\ \frac{3K_{NL}|\varphi_2|^2}{4} + \frac{1}{4\pi|\varphi_2|} \left[\left(-8\delta K_L \sqrt{1 - \frac{\delta^2}{|\varphi_2|^2}} \right) \right. \\ \left. + K_{NL} \left(-6\delta|\varphi_2|^2 \sqrt{1 - \frac{\delta^2}{|\varphi_2|^2}} + 12\delta^3 \sqrt{1 - \frac{\delta^2}{|\varphi_2|^2}} \right) \right. \\ \left. + (8K_L|\varphi_2| - 6K_{NL}|\varphi_2|^3) \arccos\left(\frac{\delta}{|\varphi_2|}\right) \right] & \text{if } |\varphi_2| \geq \delta \end{cases} \quad (12)$$

The first equation of (11) implies that $\varphi_1 = \varphi_1(\tau_1, \tau_2, \dots)$, validating for this variable the hypothesis made for use of Galerkin's method (Eq. (9)). For the second equation of (11), we seek the fixed point φ_2 verifying $\lim_{\tau_0 \rightarrow \infty} \frac{\partial\varphi_2}{\partial\tau_0} = 0$. From that, we obtain the SIM as follows:

$$\mathcal{H} = -i\varphi_2 + i\varphi_1 + i\varphi_2g(|\varphi_2|^2) - \zeta_2\varphi_2 = 0 \quad (13)$$

Expressing the complex variables of Manevitch in the polar domain as $\varphi_j = N_j e^{i\theta_j}$, $N_j \in \mathbb{R}_+$, $\theta_j \in \mathbb{R}$, $j = 1, 2$, we obtain the final equation of the SIM as follows:

$$N_1 = N_2 \sqrt{(1 - g(N_2^2))^2 + \zeta_2^2} \quad (14)$$

From this equation, it is evident that the SIM does not depend on the amplitude of the external excitation applied to the main system. In other words, the SIM is a geometrical representation of all possible final states of the system. Thus, the behavior of a system is attracted by its SIM and evolves around it. Figure 2 shows an example of SIM with its stability borders of the non-optimized system considering the parameters of Tables 1 and 2 [18].

ζ_1	ζ_2	γ
0.1	0.1	0

Table 1: Parameters of the system.

k_{NL}	k_L	δ
0.1	0.1	5

Table 2: Parameters of the restoring force function.

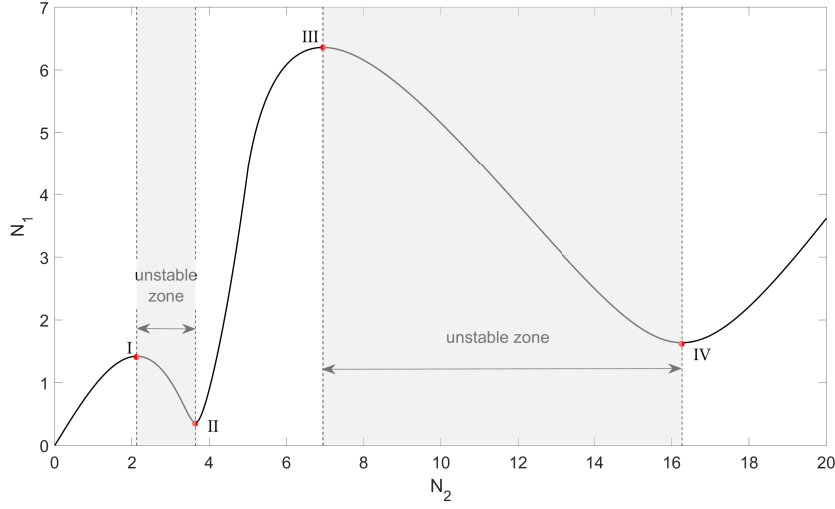


Figure 2: The SIM of a non-optimized system and its stability borders (- - -) [18].

100 *Slow dynamics.* The system behavior at the slow time scale is described by the system of equations (10) at ϵ^1 order. When the first equation of the system (10) is studied at ϵ^1 order, it yields:

$$\frac{\partial \varphi_1}{\partial \tau_1} = E_1(\varphi_1, \varphi_2, \varphi_1^*, \varphi_2^*) \quad (15)$$

where

$$E_1(\varphi_1, \varphi_2, \varphi_1^*, \varphi_2^*) = -2\sigma\varphi_1 + i\zeta_1\varphi_1 + \varphi_2 - \varphi_1 - \gamma = 0 \quad (16)$$

To detect the equilibrium and singular points of the system, Eq. 16 should be accompanied by the SIM and its evolution at τ_1 time scale, resulting in:

$$\underbrace{\begin{bmatrix} \frac{\partial \mathcal{H}}{\partial \varphi_2} & \frac{\partial \mathcal{H}}{\partial \varphi_2^*} \\ \frac{\partial \mathcal{H}^*}{\partial \varphi_2} & \frac{\partial \mathcal{H}^*}{\partial \varphi_2^*} \end{bmatrix}}_{\mathbf{S}_1} \begin{bmatrix} \frac{\partial \varphi_2}{\partial \tau_1} \\ \frac{\partial \varphi_2^*}{\partial \tau_1} \end{bmatrix} = - \underbrace{\begin{bmatrix} \frac{\partial \mathcal{H}}{\partial \varphi_1} & \frac{\partial \mathcal{H}}{\partial \varphi_1^*} \\ \frac{\partial \mathcal{H}^*}{\partial \varphi_1} & \frac{\partial \mathcal{H}^*}{\partial \varphi_1^*} \end{bmatrix}}_{\mathbf{S}_2} \begin{bmatrix} E_1 \\ E_1^* \end{bmatrix} \quad (17)$$

To determine the equilibrium points of the system, the following conditions are established:

$$\begin{cases} E_1(\varphi_1, \varphi_2, \varphi_1^*, \varphi_2^*) = 0 \\ \mathcal{H}(\varphi_1, \varphi_2, \varphi_1^*, \varphi_2^*) = 0 \\ \det(\mathbf{S}_1) \neq 0 \end{cases} \quad (18)$$

105 For the identification of singular points, the conditions are modified as follows:

$$\begin{cases} E_1(\varphi_1, \varphi_2, \varphi_1^*, \varphi_2^*) = 0 \\ \mathcal{H}(\varphi_1, \varphi_2, \varphi_1^*, \varphi_2^*) = 0 \\ \det(\mathbf{S}_1) = 0 \end{cases} \quad (19)$$

Considering Eq. (13) that links the variables φ_1 and φ_2 in the governing equation of the SIM, Eq. (16) reads to:

$$(-2\sigma + i\zeta_1 - 1)(\varphi_2 - g(N_2^2) - i\zeta_2\varphi_2) + \varphi_2 - \gamma = 0 \quad (20)$$

Upon expressing Eq. (20) in the polar domain, it can be reorganized as:

$$\begin{aligned} & (4N_2^2 - 8N_2^2g(N_2^2) + 4N_2^2g^2(N_2^2) + 4N_2^2\zeta_2^2)\sigma^2 \\ & + (-4N_2^2g(N_2^2) + 4N_2^2g^2(N_2^2) + 4N_2^2\zeta_2^2)\sigma \\ & + N_2^2(\zeta_1^2\zeta_2^2 + g^2(N_2^2) + \zeta_1^2 - 2\zeta_1g(N_2^2) + 2\zeta_1\zeta_2 + \zeta_1^2g^2(N_2^2) + \zeta_2^2) - \gamma^2 = 0 \end{aligned} \quad (21)$$

Equation 21 allows us to derive the frequency response curve in terms of N_2 for a given amplitude of forcing γ . Subsequently, the frequency response curve in terms of N_1 can be acquired using the equation of the SIM (refer to Eq. (14)).

110 Figure 3 presents an example of frequency response curves. It illustrates all possible equilibrium points for the forcing amplitude $\gamma = 2$ in terms of N_1 and N_2 , and as a function of the detuning parameter σ . The equilibrium points located in unstable zones of the SIM (presented in Fig. 2) are highlighted in green, and the isola in red. It is important to mention that if the system has only one equilibrium point and it is situated in the unstable zone, it will present modulated response [44, 45], represented by relaxation oscillations between stable branches of the SIM.

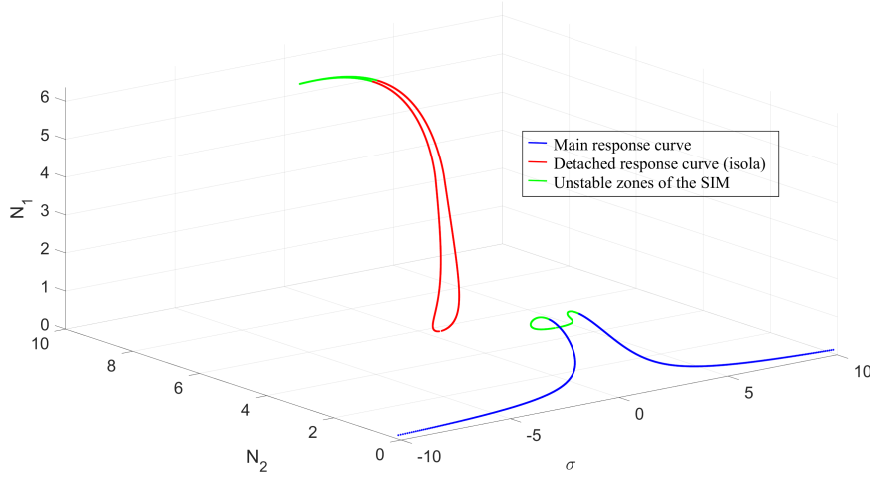


Figure 3: Detected equilibrium points of the system subjected to a forcing amplitude $\gamma = 2$ with respect to the detuning parameter σ . System parameters are provided in Tables 1 and 2 [18].

115

2.4. Activation levels

Depending on the initial conditions, the studied system exhibits the possibility of two, one, or no bifurcations for free responses. In other words, specific activation levels must be surpassed for unforced systems to exhibit bifurcations.

120 For a better understanding, numerical responses of an unforced system are added to the SIM in Fig. 4. In Fig. 4a, it is noticed that starting from the initial conditions represented by \times , the system response is attracted by the SIM. Subsequently, double bifurcations occur due to the existence of two unstable zones in the SIM (as shown in Fig. 2), leading the system to eventually reach the rest position, as expected for a damped free response. However, in Fig. 4b, the system exhibits only one bifurcation due to its lower initial condition. In contrast, in Fig. 4c, no bifurcation is observed since the initial conditions are below the bifurcations thresholds.

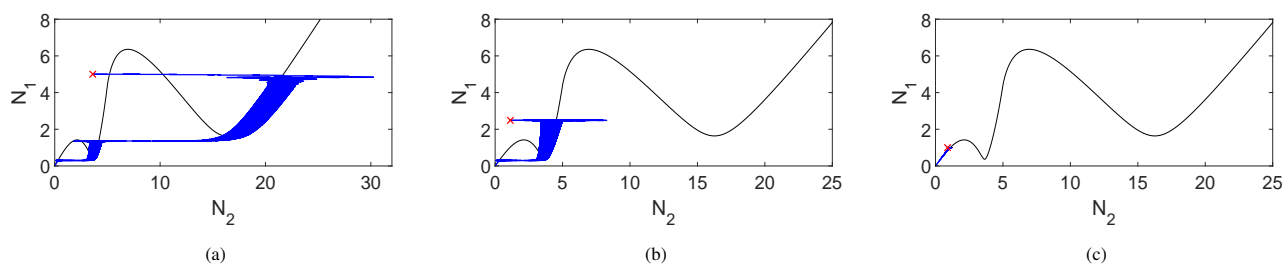


Figure 4: The SIM of the system (in black) and corresponding free numerical responses (in blue) obtained for different initial conditions represented by \times symbol: (a) $(u_{1,0}, u_{2,0}, \dot{u}_{1,0}, \dot{u}_{2,0}) = (0, 0, 4.38, 0)$; (b) $(u_{1,0}, u_{2,0}, \dot{u}_{1,0}, \dot{u}_{2,0}) = (0, 0, 2.98, 0)$; (c) $(u_{1,0}, u_{2,0}, \dot{u}_{1,0}, \dot{u}_{2,0}) = (0, 0, 0.52, 0)$. Numerical results are obtained from direct numerical integration of Eq. (3).

125

2.5. Sources of incertitudes

One of the sources of incertitudes in the response of the studied system lies in its initial conditions, such as the initial velocity of the external mass \dot{u}_1 , where the main mass is subjected to an impulse. Depending on the initial values of \dot{u}_1 , the system can exhibit one, two, or no bifurcations, as illustrated in Figure 4.

130 Another source of incertitudes is the external force applied to the outer mass. Depending on its amplitude γ and its frequency detuning parameter σ , this force can activate different parts of the SIM resulting in periodic or non-periodic responses with possible bifurcations around one or both unstable zones of the SIM.

135 It is possible to determine which part of the SIM is activated when we examine the frequency response curve on the $N_1 - N_2$ plane. The two-dimensional representation of Fig. 3 in terms of N_1 and N_2 is depicted in Fig. 5a. To complement this representation, Fig. 5b illustrates the corresponding regions of the SIM that are activated by the particular amplitude of force considered, i.e., γ parameter. It is important to note that altering the forcing amplitude activates different regions of the SIM. For instance, as the amplitude of force increases, more zones of the SIM become activated.

140 Other two-dimensional views of Fig. 3 are presented in Figs. 6a and 6b. These visual representations offer valuable insights into the system's behavior with respect to the detuning parameter (σ) of the excitation frequency. One remarkable observation is that the system can exhibit multiple possible equilibrium points for certain detuning parameters. Also, depending on this parameter, the equilibrium point can reside within a stable or unstable region of the SIM. The latter is highlighted in green and can result in a non-periodic response.

145 It is important to acknowledge that design variables, such as the parameters of the restoring force, can be sources of incertitudes when the studied system is fabricated. In the works of Boroson et al. [46, 38], the nonlinear stiffness is considered as a stochastic design variable. However, in this study, only the external force and the initial velocity will be considered as stochastic variables.

2.6. Efficiency metric

150 To maximize the efficiency of the inner mass in improving the behavior of the outer mass, an optimization process should be carried out. To achieve this, an efficiency metric is introduced and defined as the ratio between the responses

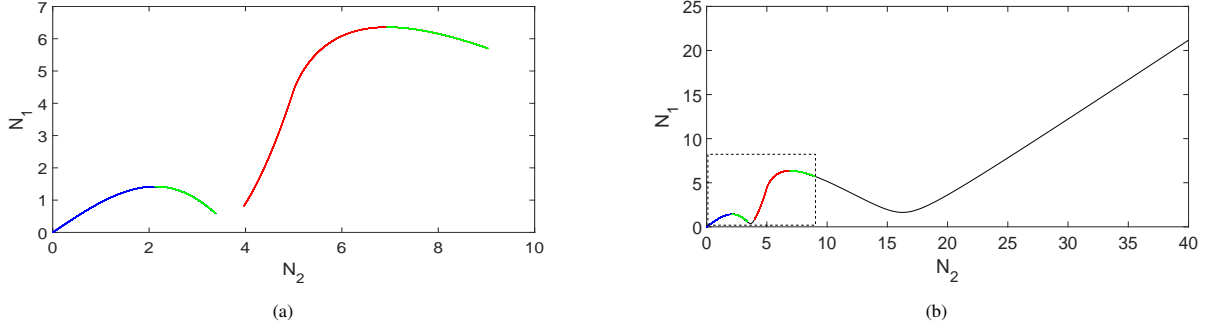


Figure 5: Two-dimensional views of Fig. 3: (a) N_1 versus N_2 ; (b) Superposition of Fig. 5a on the SIM. The system is subjected to a forcing amplitude $\gamma = 2$, with the system parameters detailed in Tables 1 and 2.

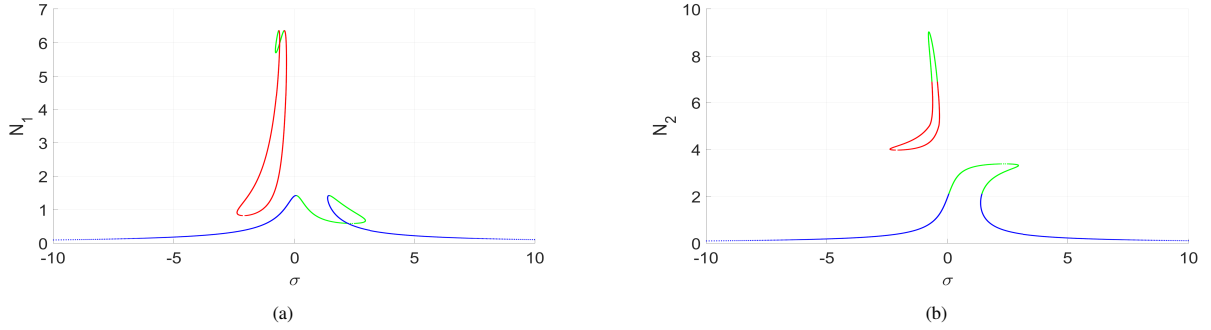


Figure 6: Two-dimensional views of Fig. 3: (a) N_1 with respect to the detuning parameter σ ; (b) N_2 with respect to σ . The system is subjected to a forcing amplitude $\gamma = 2$, with the system parameters detailed in Tables 1 and 2.

of the 2 dof, $\text{RMS}_{2dof}(\dot{u}_1)$, and the 1 dof (i.e., without inner mass), $\text{RMS}_{1dof}(\dot{u}_1)$, systems. This ratio is evaluated based on the root mean squares of \dot{u}_1 , representing the velocity of the external mass. This metric is expressed as:

$$\text{RMS}_{\dot{u}_1}^* = \frac{\text{RMS}_{2dof}(\dot{u}_1)}{\text{RMS}_{1dof}(\dot{u}_1)} \quad (22)$$

This metric quantifies the efficiency of energy reduction in the 2 dof system compared to the 1 dof system. Consequently, smaller values of $\text{RMS}_{\dot{u}_1}^*$ indicate higher efficiency in vibratory energy reduction for the 2 dof system.

2.7. Potential discontinuous behavior

As we have seen in the previous sections, the studied system can or not face bifurcations, which leads to a potential discontinuous behavior. The discontinuous behavior is evident when considering an unforced system. However, the behavior can become more complex in the case of a forced system, as we will see.

To facilitate the visualization of the distribution and patterns of the efficiency metric, histograms are generated by obtaining efficiency metric's values for a range of parameters. The values are then divided into intervals (bins), and the number of data points in each bin is quantified. Finally, these quantifications are graphically represented as bars. In Figure 7, histograms of the efficiency metric are presented, considering responses from the unforced system. The only varying initial condition is the initial velocity of the outer mass ($\dot{u}_{1,0}$), with all other initial conditions set to zero. The values of other parameters remain fixed according to Tables 1 and 2.

In Fig. 7a, the range of $\dot{u}_{1,0}$ extends from 0.5 to 2.5 and two data clusters, namely C_1 and C_2 , are distinguished: C_1 displays high values of the efficiency metric, indicating an absence of bifurcation in the system's response, and C_2 displays lower values, representative of the system's responses exhibiting one bifurcation. Upon further expansion of the range of $\dot{u}_{1,0}$ to include values from 0.5 to 5, the histogram in Fig. 7b illustrates the emergence of an additional

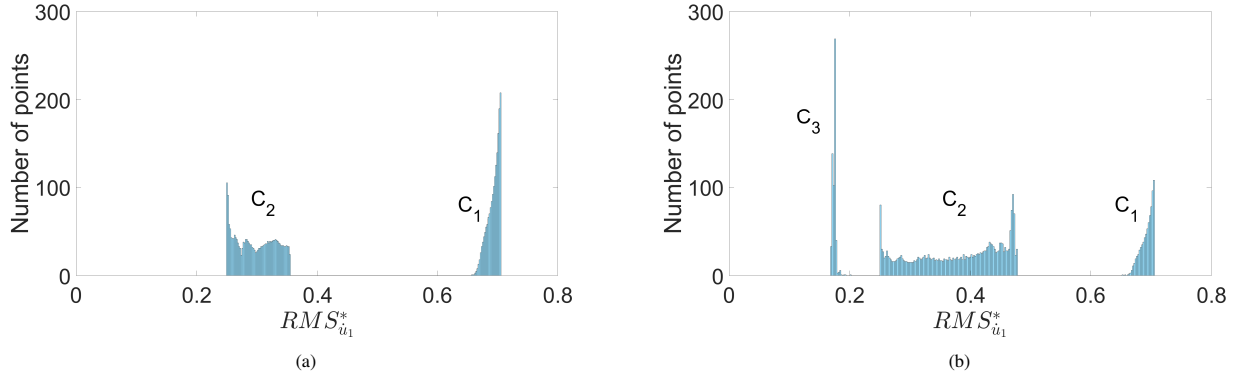


Figure 7: Histogram of the unforced system's responses: (a) $\dot{u}_{1,0} \in [0.5, 2.5]$; (b) $\dot{u}_{1,0} \in [0.5, 5]$. Different response clusters are denoted by C_1 , C_2 and C_3 .

response cluster C_3 featuring two bifurcations. One representative example for each cluster of Fig. 7b is depicted in Fig. 8.

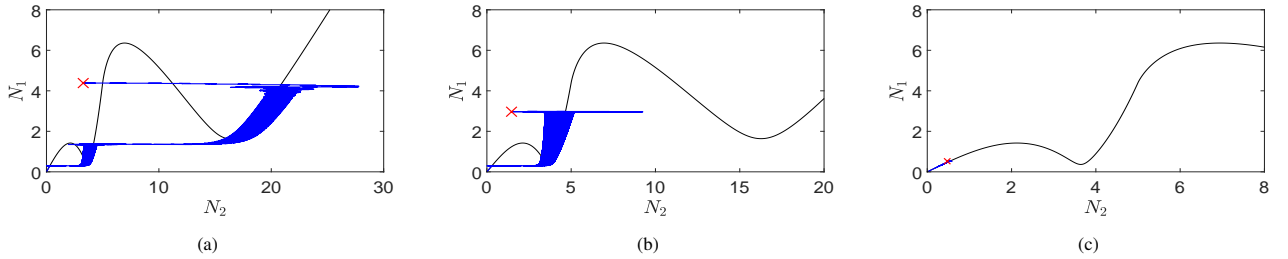


Figure 8: The SIM of the system (in black) and corresponding numerical responses of the unforced system (in blue) originating from the distinct clusters of Fig. 7b are depicted with different initial conditions represented by \times symbol: (a) $(u_{1,0}, u_{2,0}, \dot{u}_{1,0}, \dot{u}_{2,0}) = (0, 0, 4.38, 0)$ (cluster C_3 of Fig. 7b); (b) $(u_{1,0}, u_{2,0}, \dot{u}_{1,0}, \dot{u}_{2,0}) = (0, 0, 2.98, 0)$ (cluster C_2 of Fig. 7b); (c) $(u_{1,0}, u_{2,0}, \dot{u}_{1,0}, \dot{u}_{2,0}) = (0, 0, 0.52, 0)$ (cluster C_1 of Fig. 7b). Numerical results are obtained from direct numerical integration of Eq. (3).

170 In Fig. 8a, the response exhibits a double bifurcation and belongs to the cluster C_3 , characterized by the highest efficiency of the studied system compared to the 1 dof system. Figure 8b depicts a response with one bifurcation, corresponding to the cluster C_2 . Finally, Fig. 8c presents a response from the cluster C_1 , with no bifurcation, where the behavior of the studied system is closer to the behavior of the 1 dof system.

175 Figure 9 presents a histogram where, in addition to $\dot{u}_{1,0}$ ranging from 0.5 to 2.5, the parameter k_{NL} varies from 0 to 0.5 (see Eq. 5 for definition of the nonlinear restoring function). Despite the velocity ranging only from 0.5 to 2.5, as for the case presented in Fig. 7a where only two groups of responses are observed, the emergence of a third cluster C_3 below the metric's value of 0.2, i.e., $RMS_{\dot{u}_1}^* = 0.2$ (as seen in Fig. 7b), is observed due to the variation of k_{NL} .

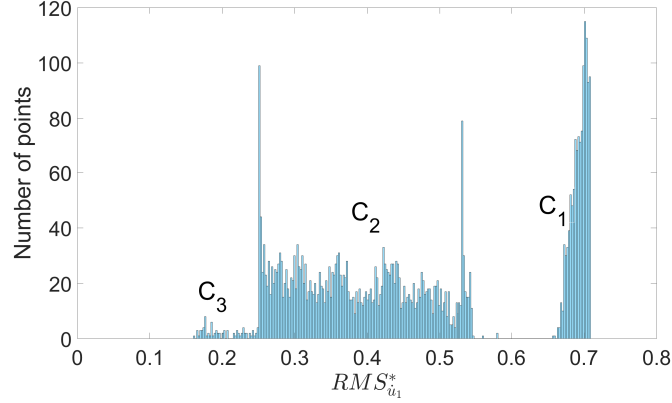


Figure 9: Histogram of the unforced system's responses: $\dot{u}_{1,0} \in [0.5, 2.5]$, $k_{NL} \in [0, 0.5]$. See Eq. 5 for definition of the nonlinear restoring function. Different response clusters are denoted by C_1 , C_2 and C_3 .

Figure 10 presents another histogram, where alongside $\dot{u}_{1,0}$ ranging from 0.5 to 2.5, the parameter δ varies from 0 to 6. Some notable differences become apparent in the histogram of Fig. 10 when compared to that of Fig. 7a: the discontinuity is less evident, and we observe the emergence of the cluster C_3 .

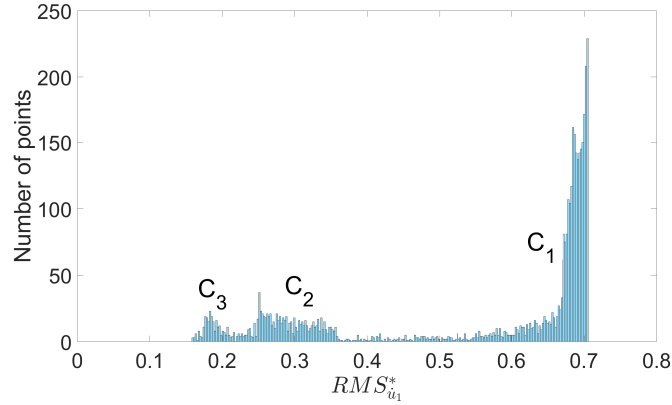


Figure 10: Histogram of the unforced system's responses: $\dot{u}_{1,0} \in [0.5, 2.5]$, $\delta \in [0, 6]$. See Eq. 5 for definition of the nonlinear restoring function. Different response clusters are denoted by C_1 , C_2 and C_3 .

To explain the difference between the histograms of Figs. 10 and 7a and their discontinuities, let us consider a set of parameters around the metric's value of 0.58 in Fig. 10, (the same value where a discontinuity is present in Fig. 7a): $\delta = 2.72$ and the initial conditions as $(u_{1,0}, u_{2,0}, \dot{u}_{1,0}, \dot{u}_{2,0}) = (0, 0, 1.58, 0)$. The corresponding SIM and numerical responses are represented in Fig. 11a. Similarly, for the same initial conditions but with $\delta = 5$ (the constant value of δ in the histogram of Fig. 7a, where the discontinuity between clusters is clear), the SIM and numerical responses are plotted in Fig. 11b. The difference between the responses in both figures is evident: in Fig. 11b, the response presents a bifurcation with a larger amplitude than the one of Fig. 11a, and thus, it is more effective in terms of energy reduction of the outer mass. In other words, varying δ causes the amplitudes of bifurcations to vary, which explains the presence of responses between the identified clusters in the histogram of Fig. 10.

In Fig. 10, cluster C_3 exhibits responses with double bifurcations, whereas cluster C_2 displays a single bifurcation. To illustrate this, a set of parameters from each cluster are selected. Figure 12b presents the numerical response and the corresponding SIM obtained using a set of parameters around the metric's value of 0.3 (cluster C_2), revealing a single bifurcation. Meanwhile, in Fig. 12a, a set of parameters around a metric's value of 0.17 (cluster C_3) are taken into account, resulting in a system's response with two bifurcations. Figure 12c presents the numerical response and

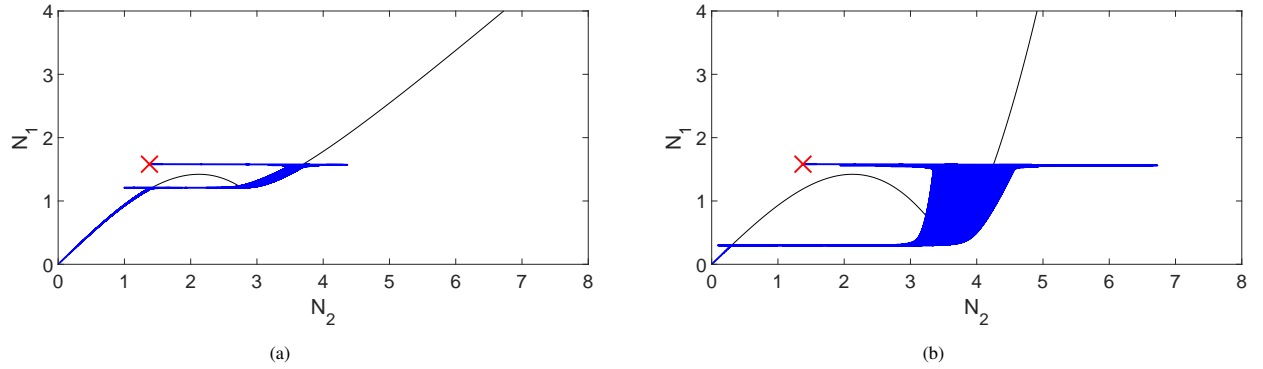


Figure 11: The SIM of the system (in black) and corresponding free numerical responses (in blue) for the initial conditions $(u_{1,0}, u_{2,0}, \dot{u}_{1,0}, \dot{u}_{2,0}) = (0, 0, 1.58, 0)$, represented by \times symbol, and: (a) $\delta = 2.72$ (between the clusters C_1 and C_2 of Fig. 10); (b) $\delta = 5$ (constant value of δ in the histogram of Fig. 7a, where the discontinuity between clusters is clear). Numerical results are obtained from direct numerical integration of Eq. (3).

the SIM of the system obtained using a set of parameters from cluster C_1 , around the metric's value of 0.7 and, as expected, this unforced response exhibits no bifurcations.

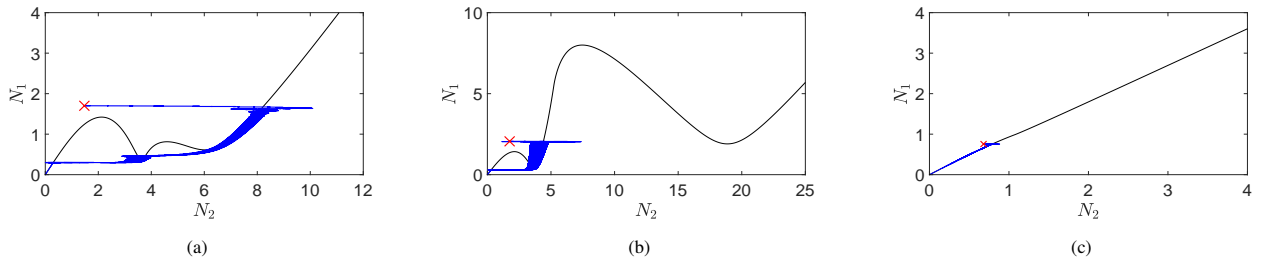


Figure 12: Numerical response of an unforced system and the SIM obtained using a set of parameters around the efficiency metric's value of (a) 0.17 (cluster C_3 of Fig. 10); (b) 0.3 (cluster C_2 of Fig. 10) and (c) 0.7 (cluster C_1 of Fig. 10). The initial conditions are represented by \times symbol. Numerical results are obtained from direct numerical integration of Eq. (3).

Figure 13 presents a histogram of the efficiency metric considering the responses of a forced system with all initial conditions set to zero (including $\dot{u}_{1,0} = 0$). Here, the amplitude of the external force γ varies from 0 to 2, and the detuning parameter σ from -1 to 1. In this case, it is difficult to distinguish different groups of efficiency metric. In fact, due to the initial conditions set to zero, it is more probable that the system is attracted to equilibrium points situated on the lower part of the main branch of the frequency response curves, one of which is illustrated for $\gamma = 2$ in Fig. 3. In other words, the system is less likely to face regimes positioned on the isola.

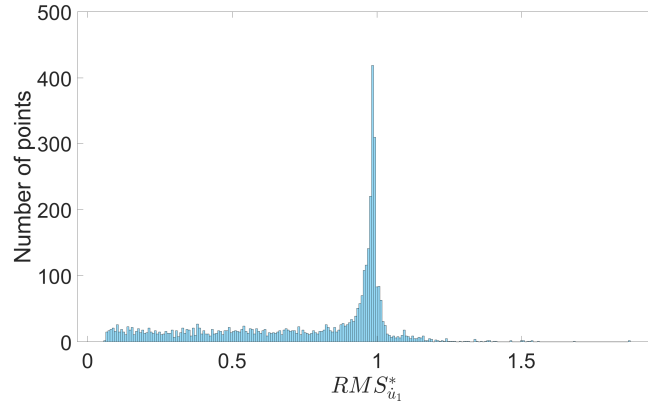


Figure 13: Histogram of the forced system's responses: $\gamma \in [0.01, 2]$, $\sigma \in [-1, 1]$.

However, if the initial velocity $u_{1,0}$ is considered in addition to γ and σ , the system's response can reach an isola and, thus, present a discontinuous behavior. To exemplify this, Fig. 14 depicts a histogram of the efficiency metric, with $\dot{u}_{1,0}$ ranging from 0.5 to 2.5 and γ ranging from 0.01 to 2. After analyzing Fig. 6, the value of σ is set to -1.5 to enable the system to potentially reach responses positioned on the isola. Finally, Fig. 14 shows two groups of responses: C_2 with the equilibrium points of the 2 dof system at the main branch of the frequency response curves and C_1 at the isola. In other words, when the equilibrium point is situated at the isola, it corresponds to high energy levels of the outer mass, resulting in a high value of the efficiency metric, which is associated with cluster C_1 .

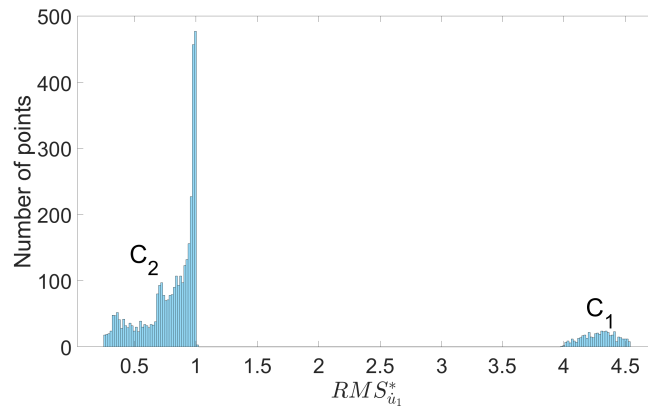


Figure 14: Histogram of the forced system's responses: $\dot{u}_{1,0} \in [0.5, 2.5]$, $\gamma \in [0.01, 2]$, $\sigma = -1.5$. Different response clusters are denoted by C_1 and C_2 .

210

3. Methodology of the stochastic optimization

3.1. Formulation of the optimization problem

The optimization problem treated in this study is written as follows:

$$\begin{aligned} \min_{\mathbf{x}_d} \quad & \mathbb{E}_{\mathbf{X}_a}(\text{RMS}_{\hat{u}_1}^*(\mathbf{x}_d, \mathbf{X}_a)) \\ \text{s.t.} \quad & \mathbf{x}_d^{\min} \leq \mathbf{x}_d \leq \mathbf{x}_d^{\max} \end{aligned} \quad (23)$$

where \mathbf{x}_d stands for design variables and \mathbf{X}_a for aleatory variables of given distribution. The design variables are the quantities to be optimized, such as the stiffnesses of the nonlinear spring. The initial conditions imposed to the system, such as initial velocities or external forces, are examples of \mathbf{X}_a . $\mathbb{E}_{\mathbf{X}_a}(\text{RMS}_{\hat{u}_1}^*)$ stands for the expected value of $\text{RMS}_{\hat{u}_1}^*$ over the aleatory variable space. The computation of the expected value is detailed in Sec. 3.3.

3.2. Space decomposition

Due to the discontinuous behavior of such system in general, the space can be divided into two regions of the design and aleatory variables using the K-means algorithm. This algorithm is employed to quantify the information gained by a given sample and to identify groups with different responses so that it minimizes the within-cluster sum of squares by moving the samples from one cluster to another [40]. In the following, the number of clusters, will be set to 2.

A Support Vector Machine (SVM) [41] is then constructed to approximate the boundary between the two classes of data (e.g., high and low efficiency) as defined by the clustering. The objective in SVM is to obtain an optimal classification boundary that maximizes the "margin." For a d -dimensional space sampled with N training points \mathbf{x}_i , the corresponding boundary that separates the two classes of data can be represented as:

$$s(\mathbf{x}) = b + \sum_{i=1}^N \lambda_i y_i K(\mathbf{x}_i, \mathbf{x}) = 0 \quad (24)$$

where b is a scalar referred to as the bias, λ_i are Lagrange multipliers, K is the kernel of the SVM, and $y_i = \pm 1$ depending on the class the point is associated with. Thus, the classification of any point \mathbf{x} is given by the sign of $s(\mathbf{x})$. The SVM boundary is first trained using a design of experiments that covers the entire space, then refined with additional samples, which is detailed in Sec. 3.4.

3.3. Response approximation and statical moment computation

Kriging meta-model [39] is an approximation (\tilde{f}) of a function (f) constructed as a trend refined by a Gaussian process:

$$\tilde{f}(\mathbf{x}) = \mu + Z(\mathbf{x}) \quad (25)$$

where μ is a trend of the model and $Z(\mathbf{x})$ is a Gaussian process of mean 0, which accounts for uncertainty in prediction depending on the sparsity of data.

The unknowns of Kriging are solved using the maximum likelihood method, constructed based on the known actual values and correlations for the evaluated samples. The main advantage of Kriging is its ability to not only offer predictions for unknown points in the design space but also provide estimates of the variance of the approximation at those points.

When the design space is divided into two regions, then two Krigings and one SVM meta-models are used to approximate the system's efficiency over the entire design and aleatory space. In this case, the expected value is computed as follows:

$$\mathbb{E}_{\mathbf{X}_a}(\text{RMS}_{\hat{u}_1}^*) = \frac{1}{N_{MC}} \sum_{i=1}^{N_{MC}} R(\mathbf{p}_i) \quad (26)$$

where R is defined as:

$$R(\mathbf{p}_i) = \begin{cases} \widetilde{\text{RMS}}_{\hat{u}_1}^{*(1)}(\mathbf{p}_i) & \text{if } s(\mathbf{p}_i) \leq 0 \\ \widetilde{\text{RMS}}_{\hat{u}_1}^{*(2)}(\mathbf{p}_i) & \text{if } s(\mathbf{p}_i) > 0 \end{cases} \quad (27)$$

\mathbf{p}_i are the N_{MC} Monte Carlo samples around \mathbf{x}_d . $\widetilde{\text{RMS}}_{\hat{u}_1}^{*(1)}$ and $\widetilde{\text{RMS}}_{\hat{u}_1}^{*(2)}$ are the Kriging approximations which depend on the classification of the sample, determined by the sign of $s(\mathbf{x})$, that is, the SVM approximation.

3.4. Adaptive sampling

In order to improve the precision of the SVM boundary, an adaptive sampling scheme referred as Generalized Max-Min (GMM) is used to refine the boundary of the failure domain. The sampling algorithm is described in detail in [47]. The objective of this algorithm is to insert a new sample as far as possible from other samples and also in the region of highest probability of misclassification by the SVM, that is, where $s(\mathbf{x}) = 0$. GMM samples are found solving the following optimization problem:

$$\begin{aligned} \mathbf{x}_g^{(k)} = \arg \max_{\mathbf{x}=\{\mathbf{x}_d, \mathbf{x}_a\}} & \mathbf{f}_{\mathbf{x}}(\mathbf{x})^{\frac{1}{(N_d+N_a)}} \min_i \|\mathbf{x} - \mathbf{x}_i\| \\ \text{s.t.} & s(\mathbf{x}) = 0 \\ & \mathbf{x}_d^{\min} \leq \mathbf{x}_d \leq \mathbf{x}_d^{\max} \\ & \mathbf{x}_a^{\min} \leq \mathbf{x}_a \leq \mathbf{x}_a^{\max} \end{aligned} \quad (28)$$

where N_d and N_a are the number of design and aleatory variables, respectively. $\mathbf{f}_{\mathbf{x}}$ is a $(N_d + N_a)$ -dimensional joint probability density function. Note that the distributions for the design variables which are assumed deterministic are uniform distributions. In addition, bounds on the aleatory variables were added as the distributions considered have a finite support.

Another adaptive sampling scheme is used to update the Krigings. The sub-problem focuses on finding the optimum in the design space without considering the aleatory variables. Among the possible choices of aleatory variables, we seek the ones that maximize the Kriging prediction's variance at the optimum $\mathbf{x}_d^{(k)}$ at the k^{th} iteration, while taking into account the joint distribution. This sub-problem can be presented as follows:

$$\begin{aligned} \mathbf{x}_a^{(k)} = \arg \max_{\mathbf{x}_a} & \mathbf{f}_{\mathbf{x}_a}(\mathbf{x}_d^{(k)}, \mathbf{x}_a)^{\frac{1}{N_a}} \hat{\sigma}^2(\mathbf{x}_d^{(k)}, \mathbf{x}_a) \\ \text{s.t.} & \mathbf{x}_a^{\min} \leq \mathbf{x}_a \leq \mathbf{x}_a^{\max} \end{aligned} \quad (29)$$

where $\hat{\sigma}^2$ is the predicted variance of the Kriging approximations at the k^{th} iteration.

3.5. Optimization algorithm

The procedure of the stochastic optimization algorithm is outlined in Algorithm 1. This algorithm is particularly employed in scenarios characterized by a discontinuous behavior, requiring the segregation of regions with markedly distinct efficiency levels. An example of such a situation is when considering the unforced system.

4. Optimization of the meta-cell

Two distinct optimization problems concerning the meta-cell are presented in this section. Firstly, the scenario takes into account the unforced system, where the outer mass is subjected to an impulse represented by its initial velocity $\dot{u}_{1,0}$. Then, a forced system is considered, with a forcing amplitude γ (see Eq. 3) and a detuning parameter of the excitation frequency σ . Across all scenarios, the damping parameters ζ_1 and ζ_2 remain fixed at 0.1, and ϵ at 0.01. The parameters governing the restoring force function of the inner mass are considered as design variables. k_{NL} and k_L range from 0 to 0.5, while δ varies from 0 to 6 (see Eq. 5 for definition of the nonlinear restoring function).

Problem I. The optimization problem considering an unforced system is formulated as:

$$\begin{aligned} \min_{\delta, k_{NL}, k_L} & \mathbb{E}_{\dot{U}_{1,0}}(\text{RMS}_{\dot{u}_1}^*(\underbrace{\delta, k_{NL}, k_L}_{\mathbf{x}_d}, \underbrace{\dot{u}_{1,0}}_{\mathbf{x}_a})) \\ \text{s.t.} & 0 \leq \delta \leq 6 \\ & 0 \leq k_{NL} \leq 0.5 \\ & 0 \leq k_L \leq 0.5 \end{aligned} \quad (30)$$

where $\dot{u}_{1,0}$ is the aleatory variable defined as $\dot{u}_{1,0} \sim \mathcal{N}_t(1.5, 0.0625)$, i.e., the variable $\dot{u}_{1,0}$ is distributed as a truncated normal distribution with mean 1.5 and variance 0.0625 (the standard deviation corresponds to 25% of the $\dot{u}_{1,0}$ ranges).

Algorithm 1 Stochastic optimization

- 1: Define an efficiency metric: $\text{RMS}_{i_1}^*$;
- 2: Generate a Design of Experiments (XDOE);
- 3: Compute the function $\text{RMS}_{i_1}^*$ (XDOE);
- 4: Divide the samples into two clusters;
- 5: Approximate the boundary between the clusters using an SVM;
- 6: Train two Kriging models, one for each cluster: $\widetilde{\text{RMS}}_{i_1}^{*(1)}$ and $\widetilde{\text{RMS}}_{i_1}^{*(2)}$;
- 7: Find the minimum $\mathbf{x}_d^{(k)}$ at the k^{th} iteration:

$$\mathbf{x}_d^{(k)} = \arg \min_{\mathbf{x}_d} \mathbb{E}_{\mathbf{x}_a} (\widetilde{\text{RMS}}_{i_1}^*(\mathbf{x}_d, \mathbf{X}_a))$$

$$\text{s.t.} \quad \mathbf{x}_d^{\min} \leq \mathbf{x}_d \leq \mathbf{x}_d^{\max}$$

- 8: Find $\mathbf{x}_a^{(k)}$ that maximizes the Kriging variance at $\mathbf{x}_d^{(k)}$ accounting for joint distribution:

$$\mathbf{x}_a^{(k)} = \arg \max_{\mathbf{x}_a} \mathbf{f}_{\mathbf{x}}(\mathbf{x}_d^{(k)}, \mathbf{x}_a) \frac{1}{N_a} \hat{\sigma}^2(\mathbf{x}_d^{(k)}, \mathbf{x}_a)$$

$$\text{s.t.} \quad \mathbf{x}_a^{\min} \leq \mathbf{x}_a \leq \mathbf{x}_a^{\max}$$

- 9: SVM refinement: generate a generalized max-min sample $\mathbf{x}_g^{(k)}$;

$$\mathbf{x}_g^{(k)} = \arg \max_{\mathbf{x}=\{\mathbf{x}_d, \mathbf{x}_a\}} \mathbf{f}_{\mathbf{x}}(\mathbf{x}) \frac{1}{(N_d+N_a)} \min_i \|\mathbf{x} - \mathbf{x}_i\|$$

$$\text{s.t.} \quad s(\mathbf{x}) = 0$$

$$\mathbf{x}_d^{\min} \leq \mathbf{x}_d \leq \mathbf{x}_d^{\max}$$

$$\mathbf{x}_a^{\min} \leq \mathbf{x}_a \leq \mathbf{x}_a^{\max}$$

- 10: Compute $\text{RMS}_{i_1}^*$ at $\mathbf{x}_g^{(k)}$ and $(\mathbf{x}_d^{(k)}, \mathbf{x}_a^{(k)})$. Add to the database;
 - 11: Repeat from *Step 4* until convergence.
-

Problem II. The optimization problem for the forced system is formulated as follows:

$$\min_{\delta, k_{NL}, k_L} \mathbb{E}_{\Gamma, \Sigma} (\text{RMS}_{i_1}^* (\underbrace{\delta, k_{NL}, k_L}_{\mathbf{x}_d}, \underbrace{\gamma, \sigma}_{\mathbf{x}_a}))$$

$$\text{s.t.} \quad 0 \leq \delta \leq 6 \tag{31}$$

$$0 \leq k_{NL} \leq 0.5$$

$$0 \leq k_L \leq 0.5$$

280 γ and σ are the aleatory variables of the problem and follow truncated normal distributions: $\gamma \sim \mathcal{N}_t(1, 0.0625)$ and $\sigma \sim \mathcal{N}_t(0, 0.0625)$. The standard deviations correspond to 25% of the aleatory variables' ranges.

Moreover, the optimization problems are conducted for the system featuring a pure cubic nonlinearity as the restoring force function of the inner mass, i.e., $f(\alpha) = k_{NL}\alpha^3$. This is carried out to establish a comparison with the scenario that involves the piecewise hybrid nonlinear-linear stiffness. The aleatory variables remain consistent with the previous 285 definitions, and the parameter k_{NL} of the restoring force is treated as the design variable, ranging from 0 to 0.5.

4.1. Results of problem I

The optimization results for an unforced system, considering two different nonlinearities (pure cubic and the hybrid nonlinearity discussed earlier), are detailed in Table 3. This table provides the optimal values of the design

290 variables, along with the number of initial samples and total iterations used in the optimization process. To verify the efficiency prediction's validity at the optimum, the table includes a comparison between the surrogate-based expected value ($\mathbb{E}_{\Sigma,\Gamma}(\widetilde{\text{RMS}}_{u_1}^*)$), i.e., determined through Kriging approximations, and the true expected values ($\mathbb{E}_{\Sigma,\Gamma}(\text{RMS}_{u_1}^*)$) derived from the actual metric using 2000 Monte Carlo samples. The table also provides the lower and upper bounds of the 95% confidence intervals (CI) of both expected values.

Parameters	Pure cubic nonlinearity	Hybrid nonlinearity
Number of Krigings	2	2
Initial DOE size	10	20
Iterations	16	17
k_{NL}	0.1605	0.2618
k_L		0.2520
δ		2.4043
$\mathbb{E}_{\Sigma,\Gamma}(\widetilde{\text{RMS}}_{u_1}^*)$ (%)	0.3182	0.1856
95% CI	[0.3164, 0.3199]	[0.1850, 0.1861]
$\mathbb{E}_{\Sigma,\Gamma}(\text{RMS}_{u_1}^*)$ (%)	0.3147	0.1844
95% CI	[0.3110, 0.3184]	[0.1828, 0.1859]

Table 3: Results of the optimization problem for the unforced system using pure cubic and hybrid restoring forces.

295 The convergence behaviors of the objective function and the design variables are illustrated in Fig. 15 for the case involving cubic nonlinearity and in Fig. 16 for the system with hybrid nonlinearity. Notably, few iterations are necessary to converge to the optimal solution. The approximations of the expected values exhibit a high level of accuracy, deviating by 2% from the actual values for each problem.

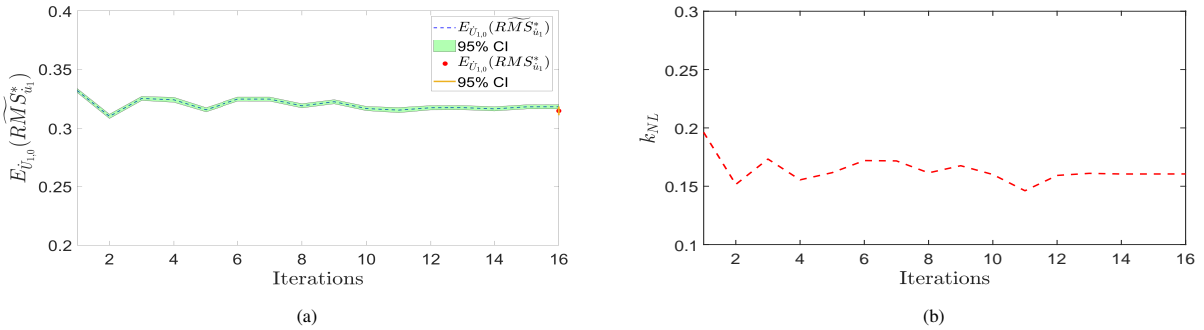


Figure 15: Optimization of the unforced 2 dof system with pure cubic restoring force. Convergences of (a) Objective function and (b) k_{NL} .

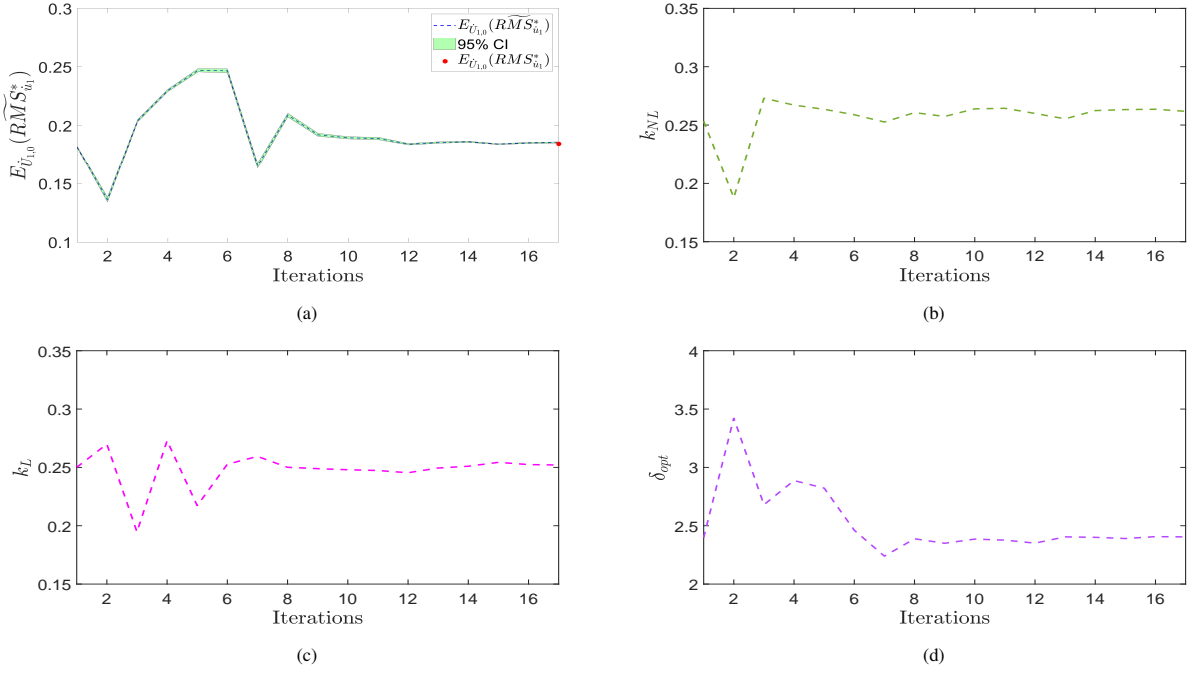


Figure 16: Optimization of the forced 2 dof system with a hybrid restoring force. Convergences of (a) Objective function; (b) k_{NL} ; (c) k_L and (d) δ .

It is worth noting that the expected value for the system with hybrid nonlinearity is significantly lower than that of the system with pure cubic nonlinearity, showing a remarkable 41.8% reduction in the expected value. This highlights the superior efficiency of the hybrid nonlinearity in reducing energy for this specific problem set when compared to the use of pure cubic nonlinearity.

Here, we will explore examples of SVM and Kriging models used in the optimization of the unforced 2 dof system with pure cubic restoring force, featuring just two variables and offering a 3D visualization. For illustration, Fig. 17a presents the design of experiments and one SVM model used to classify the efficiency metric, while Fig. 17b presents the two Kriging models built using the design of experiments to approximate the efficiency metric over the entire design space. Figure 18a displays the sample points and the SVM model at the final iteration of the optimization

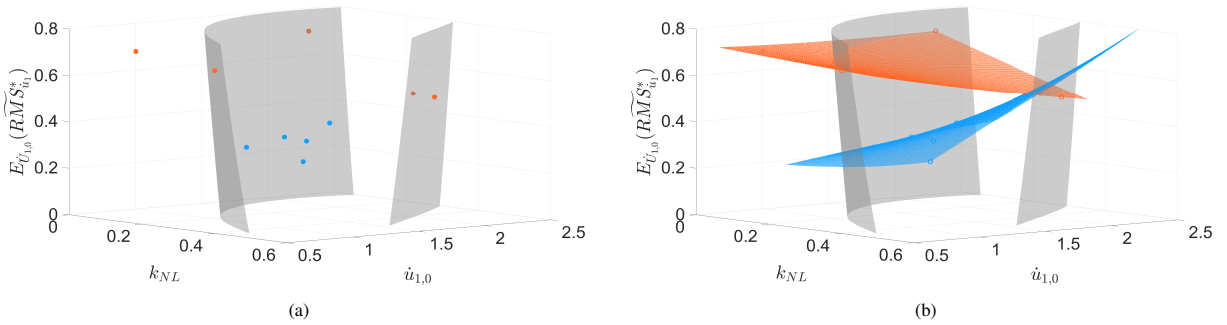


Figure 17: Models used in the optimization of the unforced 2 dof system with pure cubic restoring force function: (a) Design of experiments and SVM model; (b) SVM and Kriging models.

process. Meanwhile, Fig. 18b illustrates the two Kriging models constructed using the collected samples. Comparing Figs. 18b and 17b, we observe that the Kriging models in the last iteration (Fig. 18b) undergo a change in form due

Parameters	Pure cubic nonlinearity	Hybrid nonlinearity
Number of Krigings	1	1
Initial DOE size	15	25
Iterations	40	30
k_{NL}	0.3868	0.3574
k_L		0.3284
δ		2.0680
$\mathbb{E}_{\Sigma,\Gamma}(\widetilde{RMS}_{\dot{u}_1}^*)$ (%)	0.2528	0.2080
95% CI	[0.2489, 0.2567]	[0.2048, 0.2112]
$\mathbb{E}_{\Sigma,\Gamma}(\widetilde{RMS}_{\dot{u}_1}^*)$ (%)	0.2577	0.2115
95% CI	[0.2459, 0.2695]	[0.2047, 0.2184]

Table 4: Results of the optimization problem for the forced system using pure cubic and hybrid restoring forces.

to refinement, resulting in more precise approximations of the efficiency metric's values.

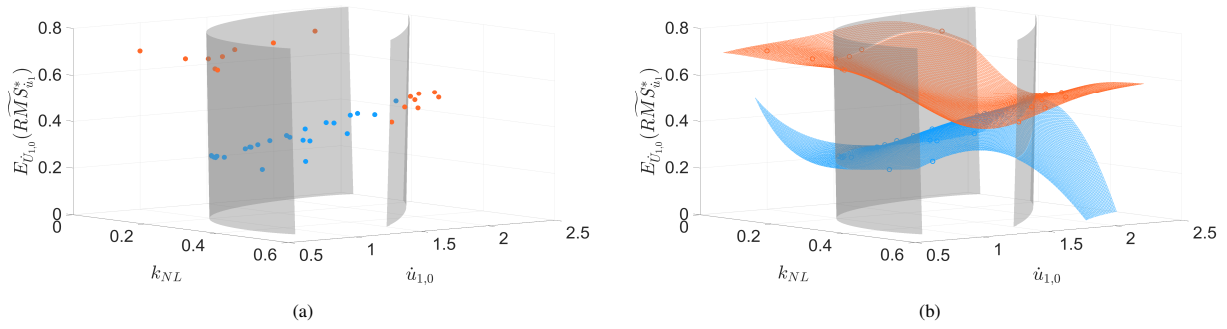


Figure 18: Models used in the optimization of the unforced 2 dof system with pure cubic restoring force function: (a) Sample points and SVM model at the final iteration; (b) SVM and Kriging models at the final iteration.

4.2. Results of the problem II

315 Table 4 presents the results and details of the optimizations of the forced systems. The convergence of the objective functions and design variables is shown in Fig. 19 for the problem with cubic nonlinearity and in Fig. 20 for the problem with hybrid nonlinearity. In both cases, relatively few iterations are required to reach the converged optimum, and the approximations of the expected values are accurate, within 2% of the actual ones for each problem.

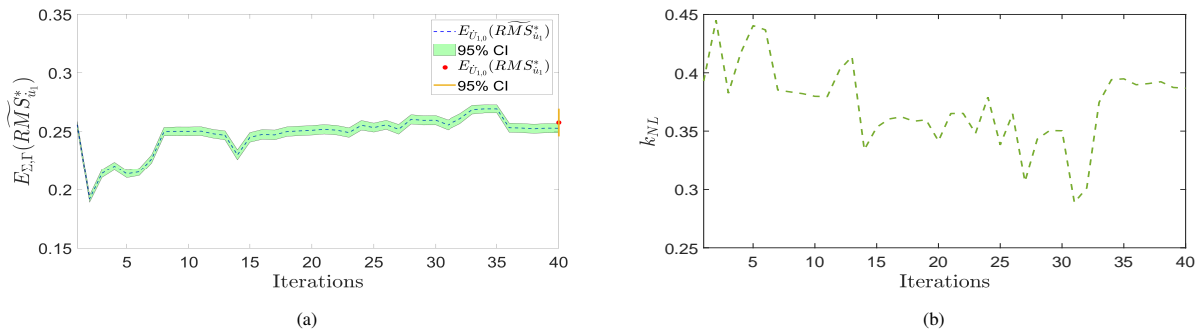


Figure 19: Optimization of the forced 2 dof system with pure cubic restoring force. Convergences of: (a) Objective function and (b) k_{NL} .

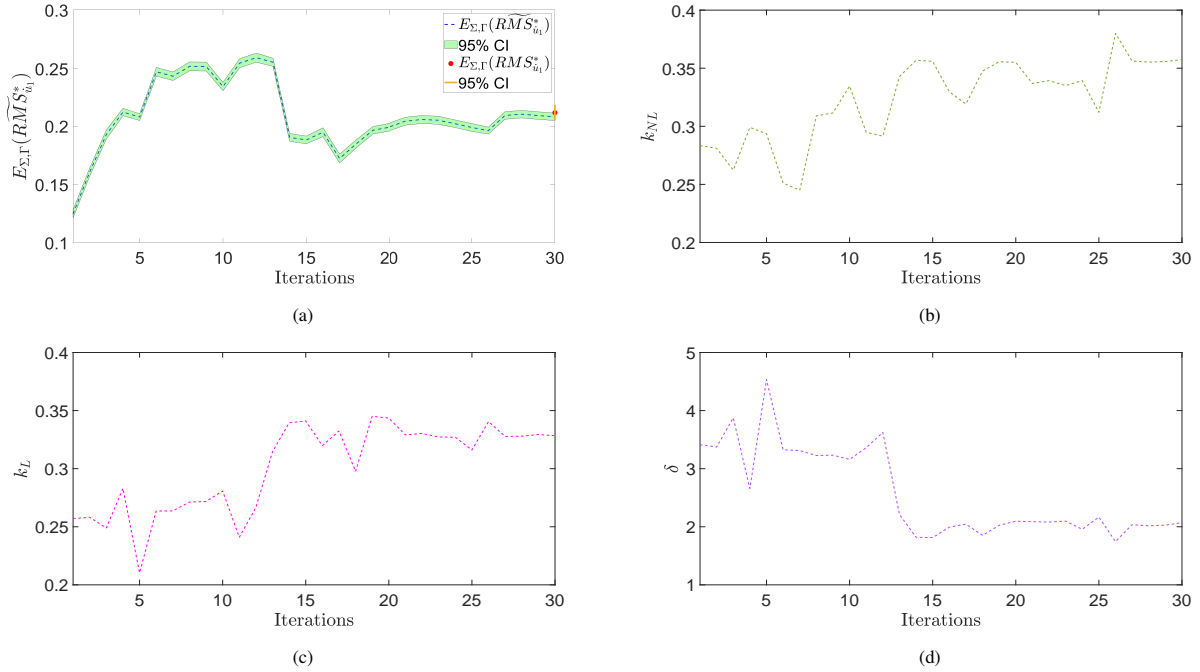


Figure 20: Optimization of the forced 2 dof system with a hybrid restoring force. Convergences of: (a) Objective function; (b) k_{NL} ; (c) k_L and (d) δ .

When comparing the expected values for both types of nonlinearities, we observe a greater reduction for the system with hybrid nonlinearity compared to the system with pure cubic nonlinearity, showing a 17.7% reduction in the expected value for this specific problem set.

Considering the 1 dof system, it is possible to trace its equilibrium points in terms of N_1 and σ . Figures 21, 22 and 23 present frequency response curves for different forcing amplitudes and systems: 1 dof, 2 dof with the optimized pure cubic nonlinearity, and 2 dof with the optimized hybrid nonlinearity. From these figures, it is clear that the curve corresponding to the hybrid nonlinearity can intersect with the other two, but it predominantly stays beneath them. In detail, we notice that the curves representing the 2 dof systems are significantly lower than the 1 dof curve, indicating a notably higher efficiency in energy reduction of the outer mass (N_1) with the addition of the inner mass, as expected, given that this additional mass works as a NES for the outer mass. When comparing the curves of hybrid and pure cubic nonlinearity, we see occasional overlap, but the hybrid nonlinearity curve is generally slightly lower than the pure cubic nonlinearity curve. Furthermore, an isola emerges in the system with pure cubic nonlinearity under the considered excitation parameters in the optimization problem. In contrast, this isola does not manifest in the system with hybrid nonlinearity. These observations justify the observed 17.7% reduction in the expected value when employing the hybrid nonlinearity.

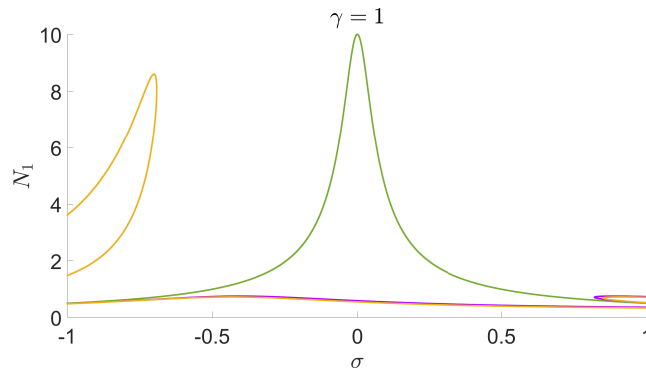


Figure 21: Frequency response curves for different systems: 1 dof system (green curve), 2 dof system with pure cubic nonlinearity (yellow curve), and 2 dof system with hybrid nonlinearity (purple curve). The curves illustrate variations in N_1 and σ for $\gamma = 1$.

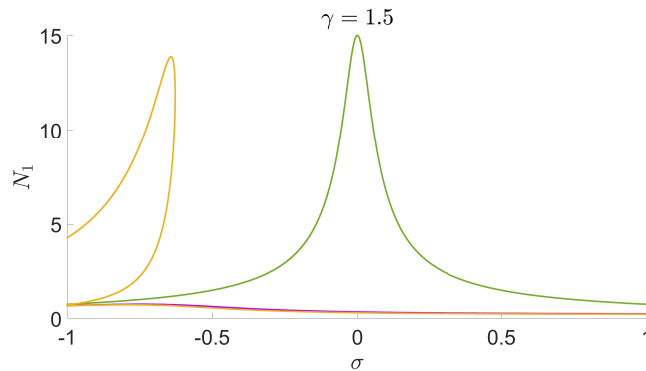


Figure 22: Frequency response curves for different systems: 1 dof system (green curve), 2 dof system with pure cubic nonlinearity (yellow curve), and 2 dof system with hybrid nonlinearity (purple curve). The curves illustrate variations in N_1 and σ for $\gamma = 1.5$.

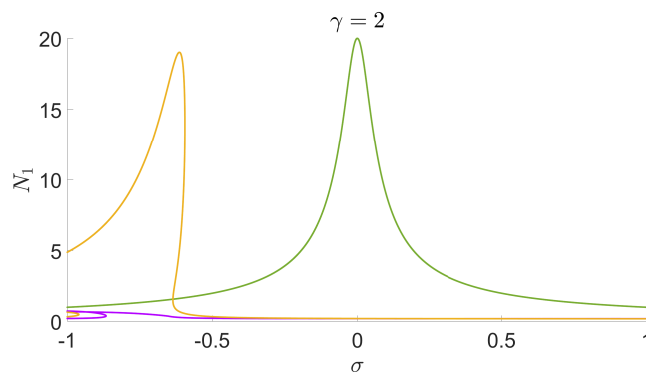


Figure 23: Frequency response curves for different systems: 1 dof system (green curve), 2 dof system with pure cubic nonlinearity (yellow curve), and 2 dof system with hybrid nonlinearity (purple curve). The curves illustrate variations in N_1 and σ for $\gamma = 2$.

5. Conclusion

335 In this paper, the stochastic optimization problem of a mass-in-mass cell is carried out. Tools such as Slow Invariant Manifolds and nonlinear frequency responses curves obtained from detection of fast and slow systems dynamics are presented to enhance the comprehension of the system's dynamic behavior, including potential discontinuities. Recognizing the system's high sensitivity to uncertainties, a stochastic optimization algorithm is employed to account

340 for them. The meta-cell with hybrid and pure cubic nonlinearities is studied, considering not only an impulse as excitation but also harmonic forces. The results demonstrate that the system with optimized hybrid nonlinearity exhibits higher efficiencies in energy reduction than the corresponding optimized pure cubic nonlinearity. The presented optimization process in this study can be applied to the design and fabrication of the considered meta-cells, aiming to enhance the efficiency of vibratory energy exchanges between two masses.

345 [In this study, a deterministic and fixed damping parameter is used for the system. Given its impact on the system's behavior, future work will involve treating the damping parameter as a design variable.](#) Additionally, optimizing a chain of mass-in-mass cells should be explored to enhance vibratory energy transfer between oscillators and different modes within the chain.

Acknowledgments

350 The authors gratefully thank the LABEX CELYA (ANR-10-LABX-0060) of the Université de Lyon for supporting this research work within the program "Investissement d'Avenir"(ANR-11-IDEX-0007) operated by the French National Research Agency (ANR).

References

- [1] E. Shamonina, L. Solymar, *Metamaterials: How the subject started*, *Metamaterials* 1 (1) (2007) 12–18. doi:<https://doi.org/10.1016/j.metmat.2007.02.001>.
- 355 [2] S. A. Tretyakov, A personal view on the origins and developments of the metamaterial concept, *Journal of Optics* 19 (1) (2016) 013002. doi:[10.1088/2040-8986/19/1/013002](https://doi.org/10.1088/2040-8986/19/1/013002). URL <https://doi.org/10.1088/2040-8986/19/1/013002>
- [3] A. O. Krushynska, D. Torrent, A. M. Aragón, R. Ardito, O. R. Bilal, B. Bonello, F. Bosia, Y. Chen, J. Christensen, A. Colombi, S. A. Cummer, B. Djafari-Rouhani, F. Fraternali, P. I. Galich, P. D. Garcia, J.-P. Groby, S. Guenneau, M. R. Haberman, M. I. Hussein, S. Janbaz, N. Jiménez, A. Khelif, V. Laude, M. J. Mirzaali, P. Packo, A. Palermo, Y. Pennec, R. Picó, M. R. López, S. Rudykh, M. Serra-García, C. M. S. Torres, T. A. Starkey, V. Tournat, O. B. Wright, Emerging topics in nanophononics and elastic, acoustic, and mechanical metamaterials: an overview, *Nanophotonics* 12 (4) (2023) 659–686 [cited 2023-03-05]. doi:[doi:10.1515/nanoph-2022-0671](https://doi.org/10.1515/nanoph-2022-0671). URL <https://doi.org/10.1515/nanoph-2022-0671>.
- 360 [4] X. Fang, J. Wen, B. Bonello, J. Yin, D. Yu, Wave propagation in one-dimensional nonlinear acoustic metamaterials, *New Journal of Physics* 19 (5) (2017) 053007. doi:[10.1088/1367-2630/aa6d49](https://doi.org/10.1088/1367-2630/aa6d49).
- [5] X. Yu, J. Zhou, H. Liang, Z. Jiang, L. Wu, Mechanical metamaterials associated with stiffness, rigidity and compressibility: A brief review, *Progress in Materials Science* 94 (2018) 114–173. doi:<https://doi.org/10.1016/j.pmatsci.2017.12.003>. URL <https://www.sciencedirect.com/science/article/pii/S0079642517301445>
- 365 [6] S. C. L. Fischer, L. Hillen, C. Eberl, Mechanical metamaterials on the way from laboratory scale to industrial applications: Challenges for characterization and scalability, *Materials* 13 (16). doi:[10.3390/ma13163605](https://doi.org/10.3390/ma13163605).
- [7] K. Bertoldi, P. M. Reis, S. Willshaw, T. Mullin, Negative poisson's ratio behavior induced by an elastic instability, *Advanced Materials* 22 (3) (2010) 361–366. doi:<https://doi.org/10.1002/adma.200901956>.
- [8] K. Bertoldi, V. Vitelli, M. Christensen, van Hecke, Flexible mechanical metamaterials, *Nature Reviews Materials* 2 (11) (2017) 17066. doi:<https://doi.org/10.1038/natrevmats.2017.66>.
- 375 [9] D. Misseroni, P. P. Pratapa, K. Liu, G. H. Paulino, Experimental realization of tunable poisons ratio in deployable origami metamaterials, *Extreme Mechanics Letters* 53 (2022) 101685. doi:<https://doi.org/10.1016/j.eml.2022.101685>. URL <https://www.sciencedirect.com/science/article/pii/S2352431622000451>
- [10] R. Zivieri, On negative effective mass and negative group velocity in anharmonic seismic metamaterials, *EPJ Applied Metamaterials* 9 (2022) 10. doi:[10.1051/epjam/2022008](https://doi.org/10.1051/epjam/2022008).
- 380 [11] M. Ruzzene, F. Scarpa, Directional and band-gap behavior of periodic auxetic lattices, *physica status solidi (b)* 242 (3) (2005) 665–680. doi:<https://doi.org/10.1002/pssb.200460385>.
- [12] J. Cha, C. Daraio, Electrical tuning of elastic wave propagation in nanomechanical lattices at mhz frequencies, *Nature Nanotechnology* 13 (11) (2018) 1016–1020. doi:<https://doi.org/10.1038/s41565-018-0252-6>.
- 385 [13] N. H. Vo, T. M. Pham, H. Hao, K. Bi, W. Chen, A reinvestigation of the spring-mass model for metamaterial bandgap prediction, *International Journal of Mechanical Sciences* 221 (2022) 107219. doi:[10.1016/j.ijmecsci.2022.107219](https://doi.org/10.1016/j.ijmecsci.2022.107219).
- [14] L. Cveticanin, M. Zukovic, Negative effective mass in acoustic metamaterial with nonlinear mass-in-mass subsystems, *Communications in Nonlinear Science and Numerical Simulation* 51 (2017) 89–104. doi:<https://doi.org/10.1016/j.cnsns.2017.03.017>. URL <https://www.sciencedirect.com/science/article/pii/S1007570417300953>
- 390 [15] J. A. D. Wattis, Breather modes of fully nonlinear mass-in-mass chains, *Phys. Rev. E* 105 (2022) 054212. doi:[10.1103/PhysRevE.105.054212](https://doi.org/10.1103/PhysRevE.105.054212). URL <https://link.aps.org/doi/10.1103/PhysRevE.105.054212>
- [16] H. Ahmed, R. Ahmed, A Mass-In-Mass Metamaterial Design for Harvesting Energy at a Broadband Frequency Range, *Energies* 16 (16) (2023) 5883. doi:[10.3390/en16165883](https://doi.org/10.3390/en16165883).
- 395 [17] H. H. Huang, C. T. Sun, Wave attenuation mechanism in an acoustic metamaterial with negative effective mass density, *New Journal of Physics* 11 (1) (2009) 013003. doi:[10.1088/1367-2630/11/1/013003](https://doi.org/10.1088/1367-2630/11/1/013003). URL <https://dx.doi.org/10.1088/1367-2630/11/1/013003>
- [18] C. da Silveira Zanin, A. Ture Savadkoohi, S. Baguet, R. Dufour, G. Hurel, Nonlinear vibratory energy exchanges in a meta-cell, *International Journal of Non-Linear Mechanics* 146 (2022) 104148. doi:[10.1016/j.ijnonlinmec.2022.104148](https://doi.org/10.1016/j.ijnonlinmec.2022.104148).
- 400 [19] J. Flosi, C. Lamarque, A. Ture Savadkoohi, Different dynamics of a periodic mass-in-mass nonlinear chain during a single mode excitation, *Meccanica* 58 (2023) 67–95. doi:[10.1007/s11012-022-01617-2](https://doi.org/10.1007/s11012-022-01617-2).
- [20] K. Ma, J. Du, Y. Liu, X. Chen, Torsional vibration attenuation of a closed-loop engine crankshaft system via the tuned mass damper and nonlinear energy sink under multiple operating conditions, *Mechanical Systems and Signal Processing* 207 (2024) 110941. doi:[10.1016/j.ymsp.2023.110941](https://doi.org/10.1016/j.ymsp.2023.110941).
- 405 [21] S. Bab, M. Najafi, J. Fathi Sola, A. Abbasi, Annihilation of non-stationary vibration of a gas turbine rotor system under rub-impact effect using a nonlinear absorber, *Mechanism and Machine Theory* 139 (2019) 379–406. doi:[10.1016/j.mechmachtheory.2019.05.005](https://doi.org/10.1016/j.mechmachtheory.2019.05.005).
- [22] H. Frahm, *Device for damping vibrations of bodies* (1909).
- [23] J. P. Den Hartog, *Mechanical Vibrations*, McGraw Hill, New York, 1934.
- [24] R. E. Roberson, Synthesis of a nonlinear dynamic vibration absorber, *Journal of Franklin Institute* 254 (1952) 205–220.
- 410 [25] O. Gendelman, L. Manevitch, A. Vakakis, R. M'Closkey, Energy pumping in nonlinear mechanical oscillators: Part I-Dynamics of the underlying hamiltonian systems, *Journal of Applied Mechanics-transactions of The Asme* 68 (2001) 34–41. doi:[10.1115/1.1345524](https://doi.org/10.1115/1.1345524).
- [26] A. Vakakis, Inducing passive nonlinear energy sinks in vibrating systems, *Journal of Vibration and Acoustics* 123 (2001) 42–48. doi:[10.1115/1.1368883](https://doi.org/10.1115/1.1368883).
- [27] A. Vakakis, O. Gendelman, Energy pumping in nonlinear mechanical oscillators: Part II-Resonance capture, *Journal of Applied Mechanics-transactions of The Asme* 68. doi:[10.1115/1.1345525](https://doi.org/10.1115/1.1345525).

- 415 [28] F. Nucera, A. Vakakis, D. McFarland, L. Bergman, G. Kerschen, Targeted energy transfers in vibro-impact oscillators for seismic mitigation, *Nonlinear Dynamics* 50 (3) (2007) 651–677, publisher: Springer.
- [29] O. Gendelman, Analytic treatment of a system with a vibro-impact nonlinear energy sink, *Journal of Sound and Vibration* 331 (2012) 4599–4608.
- 420 [30] E. Gourc, G. Michon, S. Seguy, A. Berlioz, Targeted energy transfer under harmonic forcing with a vibro-impact nonlinear energy sink: Analytical and experimental developments, *Journal of Vibration and Acoustics* 137 (3).
- [31] C.-H. Lamarque, O. Gendelman, A. Ture Savadkoohi, E. Etcheverria, Targeted energy transfer in mechanical systems by means of non-smooth nonlinear energy sink, *Acta mechanica* 221 (1) (2011) 175–200, publisher: Springer.
- [32] M. Weiss, B. Vaurigaud, A. Ture Savadkoohi, C.-H. Lamarque, Control of vertical oscillations of a cable by a piecewise linear absorber, *Journal of Sound and Vibration* 435 (2018) 281–300.
- 425 [33] G. Hurel, A. Ture Savadkoohi, C.-H. Lamarque, Design of a nonlinear absorber for a 2 degrees of freedom pendulum and experimental validation, *Structural Control and Health Monitoring* 28 (11) (2021) e2814. doi:<https://doi.org/10.1002/stc.2814>.
- [34] A. Ture Savadkoohi, C.-H. Lamarque, M. Contessa, Trapping vibratory energy of main linear structures by coupling light systems with geometrical and material non-linearities, *International Journal of Non-Linear Mechanics* 80 (2016) 3–13.
- 430 [35] S. Aubry, G. Kopidakis, A. Morgante, G. Tsironis, Analytic conditions for targeted energy transfer between nonlinear oscillators or discrete breathers, *Physica B: Condensed Matter* 296 (1-3) (2001) 222–236. doi:10.1016/S0921-4526(00)00804-8.
- [36] E. Boroson, S. Missoum, P.-O. Mattei, C. Vergez, Optimization Under Uncertainty of Nonlinear Energy Sinks, in: Volume 8: 26th Conference on Mechanical Vibration and Noise, American Society of Mechanical Engineers, Buffalo, New York, USA, 2014, p. V008T11A084. doi:10.1115/DETC2014-34238.
- 435 [37] K. Marti, Stochastic optimization methods: applications in engineering and operations research, third edition Edition, Springer, Berlin Heidelberg New York Dordrecht London, 2015. doi:10.1007/978-3-662-46214-0.
- [38] E. Boroson, S. Missoum, Stochastic optimization of nonlinear energy sinks, *Structural and Multidisciplinary Optimization* 55 (2) (2017) 633–646. doi:10.1007/s00158-016-1526-y.
- [39] N. Cressie, The origins of kriging, *Mathematical Geology* 22 (3) (1990) 239–252. doi:10.1007/BF00889887.
- 440 [40] J. A. Hartigan, M. A. Wong, Algorithm AS 136: A K-Means Clustering Algorithm, *Applied Statistics* 28 (1) (1979) 100. doi:10.2307/2346830.
- [41] N. Cristianini, J. Shawe-Taylor, An Introduction to Support Vector Machines and Other Kernel-based Learning Methods, 1st Edition, Cambridge University Press, 2000. doi:10.1017/CB09780511801389.
- [42] A. H. Nayfeh, D. T. Mook, Nonlinear oscillations, wiley classics library ed Edition, Wiley classics library, Wiley, New York, 1995.
- 445 [43] L. I. Manevitch, The Description of Localized Normal Modes in a Chain of Nonlinear Coupled Oscillators Using Complex Variables, *Nonlinear Dynamics* 25 (1) (2001) 95–109. doi:10.1023/A:1012994430793.
- [44] Y. Starosvetsky, O. Gendelman, Strongly modulated response in forced 2DOF oscillatory system with essential mass and potential asymmetry, *Physica D: Nonlinear Phenomena* 237 (13) (2008) 1719–1733. doi:10.1016/j.physd.2008.01.019.
- [45] G. Hurel, A. Ture Savadkoohi, C.-H. Lamarque, Nonlinear Vibratory Energy Exchanges between a Two-Degree-of-Freedom Pendulum and a Nonlinear Absorber, *Journal of Engineering Mechanics* 145 (8) (2019) 04019058. doi:10.1061/(ASCE)EM.1943-7889.0001620.
- 450 [46] E. Boroson, S. Missoum, P.-O. Mattei, C. Vergez, Optimization under uncertainty of parallel nonlinear energy sinks, *Journal of Sound and Vibration* 394 (2017) 451–464. doi:10.1016/j.jsv.2016.12.043.
- [47] S. Lacaze, S. Missoum, A generalized max-min sample for surrogate update, *Structural and Multidisciplinary Optimization* 49 (4) (2014) 683–687. doi:10.1007/s00158-013-1011-9.